The Aeronautical Journal (2025), **129**, pp. 2055–2081
doi:10.1017/aer.2025.19

ROYAL AERONAUTICAL SOCIETY

RESEARCH ARTICLE

Adaptive gain-scheduling control for hypersonic flight vehicles across wide envelopes based on Guardian map

T.Y. Zhang[1], M.W. Sun[1], Z.Q. Chen[1] and Y.S. Wang[2]

[1]College of Artificial Intelligence, Nankai University, Tianjin, China
[2]College of Artificial Intelligence, Tiangong University, Tianjin, China
Corresponding author: M.W. Sun; Email: smw_sunmingwei@163.com

Received: 14 September 2024; **Revised:** 7 January 2025; **Accepted:** 18 February 2025

Keywords: gain-scheduling control; linear parameter-varying; wide envelope; Guardian map

Abstract

In this study, we developed an adaptive gain-scheduling algorithm for hypersonic flight vehicles operating across wide altitude-Mach number envelopes. First, we employed a gap metric-based nominal point selection algorithm to establish a linear parameter-varying (LPV) model more accurate than the traditional Jacobian linearisation method. Active disturbance rejection control (ADRC) was then applied to cope with disturbances and uncertainties, and control gains were scheduled using the Guardian maps (GM) method to adapt to the wide envelope of velocity and altitude. The simulation results demonstrate that under all operating conditions, the proposed algorithm can automatically iterate to obtain a gain-scheduling strategy that meets the flying qualities requirements. Notably, the proposed algorithm exhibited an integral of the time absolute error approximately half of that of the traditional ADRC and significantly lower than that of the GM-LQR method in the ascent phase, demonstrating its excellent control performance and robustness.

Nomenclature

v	flight velocity (m/s)
γ	flight path angle (rad)
h	flight altitude (m)
α	angle-of-attack (rad)
q	fitch rate (rad/s)
δ_e	elevator deflection angle (rad)
β	throttle setting
T	thrust (N)
L	lift (N)
D	drag (N)
m	mass (kg)
c	mean aerodynamic chord (m)
M_y	pitching moment ($kg \cdot m^2$)
R_e	radius of the Earth (m)
r	radial distance from Earth's centre (m)
ρ	density of air (kg/m^3)
a	speed of sound (m/s)
M	mach number
I_y	moment of inertia ($kg \cdot m^2$)
μ	gravitational constant (m^3/s^2)
C_L	lift coefficient
C_D	drag coefficient

© The Author(s), 2025. Published by Cambridge University Press on behalf of Royal Aeronautical Society.

https://doi.org/10.1017/aer.2025.19 Published online by Cambridge University Press

C_T	thrust coefficient
$C_{M\alpha}$	derivative of pitching moment coefficient with respect to angle-of-attack
C_{Mq}	derivative of pitching moment coefficient with respect to pitch rate
$C_{M\delta_e}$	derivative of pitching moment coefficient with respect to elevator
ADRC	active disturbance rejection control
LPV	linear parameter varying
ITAE	integral of time absolute error
LQR	linear quadratic regulator

1.0 Introduction

Wide-envelope flight vehicles operating in near-space have attracted significant attention owing to their high flight and response speeds and outstanding manoeuverability [1,2]. These types of aircraft must manoeuver over a wide range of altitudes and speeds to meet real-time mission demands [3,4], making the flight control a challenge [5,6]. In addition, the near-space environment is complex [7], changeable and uncertain; thus, control-oriented models have large perturbation ranges and multiple disturbance sources with wide variation range [8]. However, this results in significant variations in their dynamic characteristics [9], making it difficult for a single controller to cover all operating conditions [10–12]. Therefore, there is an urgent need for a wide-envelope automatic gain-scheduling strategy for flight vehicles with model uncertainty [13,14].

To overcome unknown disturbances and uncertainties during flight, the active disturbance rejection control (ADRC) proposed by Han is widely used in aircraft attitude control [15]. ADRC employs an extended state observer (ESO) to estimate and compensate for modeling errors and nonlinear uncertainties without relying on specific mathematical models [16]. Gao simplified the initial nonlinear ADRC into linear ADRC (LADRC) to facilitate its application in practice [17,18]. Although LADRC gain scheduling within a large flight envelope is intuitive and straightforward, designing the parameter set is difficult. Therefore, there is a need for an automatic gain-scheduling strategy for wide-envelope aircraft within the active disturbance rejection control framework.

For traditional gain-scheduling control, a linear controller is designed for each operating point; thus, it is difficult to ensure global control performance. In addition, it highly depends on the selected operating points [19,20]. The linear parameter-varying (LPV) technique embeds dynamic nonlinearities in the varying parameters, explicitly accounting for the variations in real-time parameters. Recently, the LPV method has been widely used for gain-scheduling control of flight vehicles owing to its effectiveness in managing variations. Caigny [21] proposed a gain-scheduling controller based on a parametric-dependent Lyapunov function matrix. This method was successfully applied to an aircraft LPV model by solving parametric-dependent linear matrix inequalities (LMI). Kazemi [22] developed a polyhedral LPV for quadrotor aircraft with uncertainties to achieve robust attitude control. Lucas [23] proposed a sufficient stability condition for time-delayed LPV systems based on the Lyapunov–Krasovskii function. Jiang [24,25] employed the switching polyhedral linear parameter-varying (SPLPV) framework for gain scheduling of the output feedback control to ensure stability and robustness throughout the flight envelope. Vinco [26] proposed an LPV control design for guided projectiles. They used an LPV polytopic system to ensure stability and performance across the flight envelope while reducing the computational complexity of the controller synthesis. These studies have shown that converting the nonlinear model into a polytopic LPV model can effectively address the practical challenge of controller design for morphing aircraft, thereby offering significant engineering application values. The methods developed in previous studies focused on Hurwitz's stability with respect to parametric uncertainty in specific convex geometrical regions.

The Guardian map (GM) defines a scalar-valued function of parameterised matrices with a specific distribution of eigenvalues or roots known as generalised stability. Saydy [27] developed the Guardian map as a unifying tool for studying generalised stability. It can quantitatively analyse the range of scheduling variables for LPV stability and has been extensively employed in control designs owing

https://doi.org/10.1017/aer.2025.19 Published online by Cambridge University Press

to its concise algebraic representation of closed-loop performance defined by generalised stability, such as flying quality (FQ). Saussie [28] verified the effectiveness of the GM theory for robust generalised stability problems using a second-order linear model. Xiao [29–31] employed this theory to design the control law of large-envelope aircraft and achieved adaptive tuning of the control parameters. Cao [32] proposed a multimodel switching predictive control strategy based on GM to ensure successful perching maneuvers and smooth switching.

Herein, we propose a flight vehicle ADRC gain-scheduling strategy based on GM. The gap metric theory [33] was adopted to more accurately describe the discrepancy between linear systems, making the LPV model more precise and reasonable than the traditional Jacobian linearisation method. The GM was employed to calculate the initial controller gains at a boundary point. Through iterations, a controller set covering the entire flight envelope can be obtained automatically, and a controller gain-scheduling strategy can be achieved. The primary contributions of this paper are as follows:

(1) The gap metric-based nominal point selection (NPS) algorithm is used to divide the envelope and determine the linearised operating points, ensuring accurate LPV modeling while reducing computational complexity and enhancing model reliability.

(2) The GM is employed in ADRC gain scheduling, which can automatically extend the performance of an initial controller to the entire two-dimensional (2D) envelope with enhanced robustness, thereby automating the design process without manual intervention.

The remainder of this paper is organised as follows. Section 2 presents the nonlinear model for wide-envelope flight vehicles. Section 3 presents the LPV model using the gap metric. In section 4, the gain-scheduling algorithm for ADRC based on GM is proposed. Section 5 presents the simulation results, and Section 6 concludes the paper.

2.0 Longitudinal nonlinear modeling for flight vehicle

The winged-cone vehicle model, which was used in the NASA wind experiment for aerodynamic testing [34], was selected as the subject of this study. Figure 1 shows the vehicle and its control surfaces (elevon and rudder). The elevon is a combination of the elevator and aileron; thus, it performs both pitch and roll control functions. Table 1 lists its parameters. The equations of the longitudinal motion are expressed as follows [35]

$$\begin{cases} \dot{v} = \frac{T\cos\alpha - D}{m} - \frac{\mu\sin\gamma}{r^2} \\ \dot{\gamma} = \frac{L + T\sin\alpha}{mv} - \frac{\left(\mu - v^2 r\right)\cos\gamma}{vr^2} \\ \dot{h} = v\sin\gamma \\ \dot{\alpha} = q - \dot{\gamma} \\ \dot{q} = \frac{M_y}{I_y} \end{cases}, \tag{1}$$

with

$$\begin{aligned} L &= 0.5\rho v^2 s C_L \\ D &= 0.5\rho v^2 s C_D \\ T &= 0.5\rho v^2 s C_T \\ M_y &= 0.5\rho v^2 s c \left(C_{M\alpha} + C_{M\delta_e} + C_{Mq}\right) \\ r &= h + R_E \end{aligned} \tag{2}$$

where v, γ, h, α and q are the flight speed, flight path angle, flight altitude, angle-of-attack and pitch rate of the aircraft, respectively; L, D, T and M_y represent the lift, drag, thrust and pitching moments,

https://doi.org/10.1017/aer.2025.19 Published online by Cambridge University Press

Table 1. *The parameters in the model*

Notation	Values	Notation	Values
m (kg)	136, 425.63	c (m)	24.384
I_y (kg · m^2)	649, 321	S (m^2)	334.85
R_E (m)	6, 372, 907.8	μ (m^3/s^2)	3.936×10^{14}

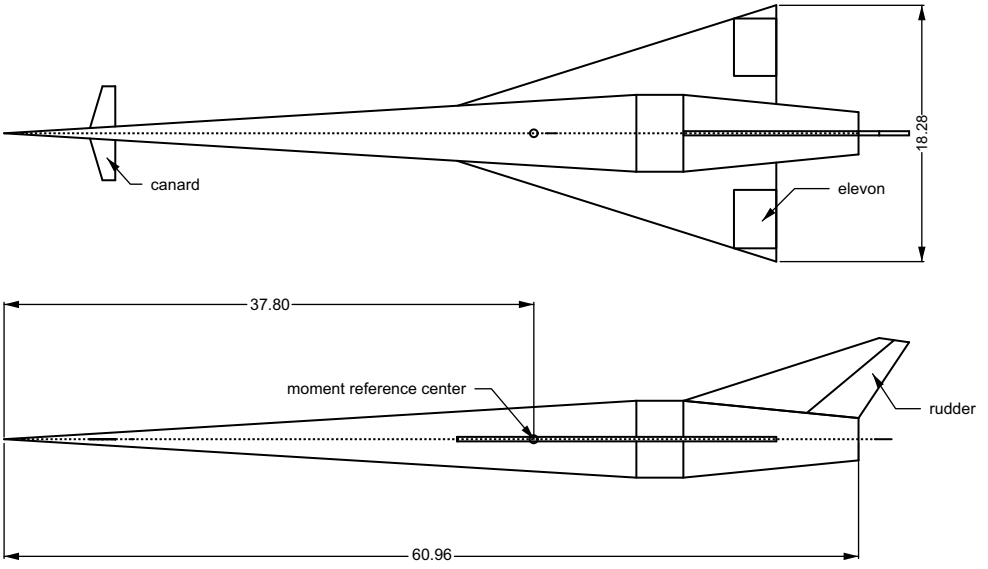


Figure 1. *Configuration geometry.*

respectively; m, I_y, μ and R_e denote the vehicle mass, longitudinal moment of inertia, gravitational constant and earth radius, respectively. C_L, C_D and C_T are the coefficients of the lift, drag, and thrust, respectively, and $C_{M\alpha}$, C_{Mq} and $C_{M\delta_e}$ are the derivatives of the pitching moment with respect to the angle-of-attack, pitch rate and elevator deflection, respectively. The variables in Equation (2) are as follows:

$$
\begin{aligned}
&\rho = 1.2244e^{-\frac{h}{7315.2}} \\
&a = 2.54 \times 10^{-10}h^2 - 8.5 \times 10^{-5}h + 303.47 \\
&M = V/a \\
&C_L = \alpha\left(0.493 + 1.91M^{-1}\right) \\
&C_D = 0.0082\left(171\alpha^2 + 1.15\alpha + 1\right)\left(0.0012M^2 - 0.054M + 1\right) \\
&C_T = \begin{cases} k\,(1 + 0.15)\,\beta, \beta < 1 \\ k\,(1 + 0.15\beta)\,, \beta \geqslant 1 \end{cases} \\
&C_{M\alpha} = 10^{-4}\left(0.06 - e^{-M/3}\right)\left(-6565\alpha^2 + 6875\alpha + 1\right) \\
&C_{M\delta_e} = 0.0292\,(\delta_e - \alpha) \\
&C_{Mq} = (c/2v)\,q\,(-0.025M + 1.37)\left(-6.83\alpha^2 + 0.303\alpha - 0.23\right).
\end{aligned}
\tag{3}
$$

The dynamic equation of the elevator actuator is expressed as follows:

$$
G_e(s) = \frac{\delta_e(s)}{\delta_c(s)} = \frac{\omega_a^2}{s^2 + 2\xi\omega_a s + \omega_a^2}, \tag{4}
$$

https://doi.org/10.1017/aer.2025.19 Published online by Cambridge University Press

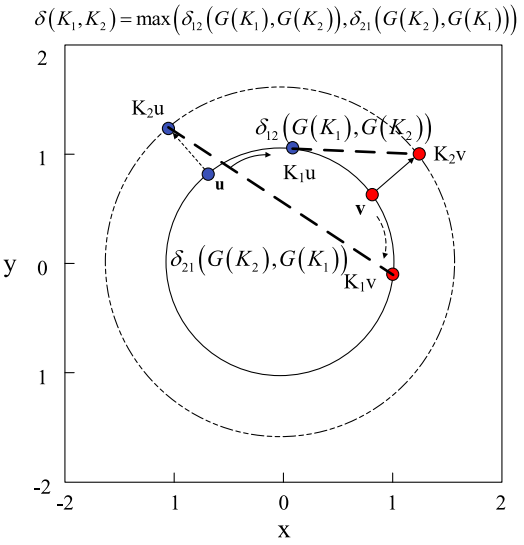


Figure 2. *Geometric representation of operators K_1 and K_2 with gap.*

where δ_c is the elevator command, δ_e the elevator deflection angle, ω_a the bandwidth and $\xi_a = 0.707$ the damping ratio.

3.0 Gap metric-based aircraft lpv modeling

3.1 Gap metric

Let K be a linear operator in Hilbert space H [33]:

$$K : H \to H. \tag{5}$$

$H \times H$ is the set of all pairs u, v; u and v are in H. $H \times H$ is also a Hilbert space with the inner product derived from H. The domain of K, $D(K)$, is the set of all u in H with the property that Ku is in H. The graph $G(K)$ of K is the set of all pairs u, Ku with u in $D(k)$ and is defined as $G(K) = \{(u, Ku) \in H \times H | u \in D(K)\}$.

Because K is linear, $G(k)$ is a subspace of the product Hilbert space $H \times H$. K is considered closed if its graph (K) is a closed subspace of $H \times H$.

Definition 1. *The gap between two closed operators K_1 and K_2 in Hilbert space H is defined as the gap between their graphs considered closed subspaces:*

$$\delta(K_1, K_2) = \delta(G(K_1), G(K_2)) = \max(\delta_{12}(G(K_1), G(K_2)), \delta_{21}(G(K_2), G(K_1))), \tag{6}$$

where $\delta_{12}(G(K_1), G(K_2)) = \sup_{u \in D(K_1), u \neq 0} \inf_{v \in D(K_2)} \frac{u - v^2 + K_1 u - K_2 v^2}{\sqrt{u^2 + K_1 u^2}}$.

$\delta_{21}(G(K_2), G(K_1))$ is defined similarly.

Example 1: *$K_1 = [\cos\theta, -\sin\theta; \sin\theta, \cos\theta]$ is a rotation by θ radians. $K_2 = [\lambda, 0; 0, \lambda]$ is a scaling by a factor of λ. u and v are the unit vectors on the unit circle $\mathbb{R}^2$. Figure 2 shows a gap $\delta(K_1, K_2)$.*

We consider linear systems as mappings in Hilbert space. For a multiinput multioutput linear system, which is represented by state matrices A and B and input matrices C and D, the transfer function is expressed as $P(s) = C(sI - A)^{-1}B + D$, where I is the identity matrix. Notably, $P(s)$ is a linear operation in Hilbert space.

https://doi.org/10.1017/aer.2025.19 Published online by Cambridge University Press

Definition 2. *If P_1 and P_2 are the transfer functions of two systems, the gap between the two systems can be expressed by the operator gap as follows:*

$$\delta_{gap}\left(P_1, P_2\right) = \max\left(\delta_{12}\left(P_1, P_2\right), \delta_{21}\left(P_2, P_1\right)\right), \tag{7}$$

where

$$\delta_{12}\left(P_1, P_2\right) = \delta\left(G\left(P_1\right), G\left(P_2\right)\right) = \Pi_{G(P_1)}, \Pi_{G(P_2)} = \inf_{Q \in H_\infty} \begin{bmatrix} M_1 \\ N_1 \end{bmatrix} - \begin{bmatrix} M_2 \\ N_2 \end{bmatrix} Q_\infty,$$

and (M_1, N_1), (M_2, N_2) represent the left prime decomposition of the linear transfer functions P_1 and P_2, respectively. Q is a Hilbert matrix.

The properties of the gap metric include the following (refer to Ref. (33,36) for more details):

(1) The gap metric is a measure of the distance between two linear systems.

(2) The gap metric lies between 0 and 1, $0 \leq \delta_{gap}\left(P_1, P_2\right) \leq 1$. The smaller the gap between the two systems, the closer their dynamic characteristics are.

3.2 Gap metric-based NPS algorithm for LPV modeling

The GM was used to analyse the generalised stability of parametric matrix families, which requires state space models. Therefore, it is crucial to develop an efficient LPV to cover nonlinear dynamics.

A nonlinear model in the LPV form can be represented using three methods: Jacobian linearisation, state transformations and function substitution [37]. Among them, Jacobian linearisation is widely used. However, it relies on a set of linearised models corresponding to several equilibrium points, which must cover the entire flight envelope to ensure good fidelity with the original nonlinear model. Therefore, to avoid choosing similar equilibrium points and reduce unnecessary computational complexity, the gap metric is introduced to measure the similarity among linear systems based on Jacobian linearisation, which is called the NPS algorithm. The NPS algorithm employs gap metric analysis to identify optimal nominal points within the sub-envelopes, ensuring accurate LPV modeling of nonlinear systems by minimising computational complexity and enhancing model fidelity.

First, the flight envelope is divided into subenvelopes according to the gap metric value. Then, a point in each subenvelope with the smallest difference in model characteristics with other state points is selected. This point is called the nominal point. Finally, the LPV model is obtained by fitting the linear model at nominal points using the following steps:

Suppose the large flight envelope is denoted as ϕ, and its range is $[M_{\min}, M_{\max}] \times [h_{\min}, h_{\max}]$.

Step 1. In the flight envelope, the average grid points are divided at certain intervals of ΔM and Δh, and a total of $N_{Ma} \times N_h$ state points are obtained.

$$\begin{cases} N_{Ma} = \left(M_{\max} - M_{\min}\right)/\Delta M + 1 \\ N_h = \left(h_{\max} - h_{\min}\right)/\Delta h + 1 \end{cases}. \tag{8}$$

Step 2. The corresponding LTI set is obtained using the Taylor series expansion method at the grid points, which can be denoted as P_{ij}, $i = 1, 2, \ldots N_{Ma}$, $j = 1, 2, \ldots N_h$.

Step 3. Calculate the gap measure between adjacent points using the expression $\delta_{gap}\left(P_{i,j}, P_{i,j+1}\right)$ or $\delta_{gap}\left(P_{i,j}, P_{i+1,j}\right)$.

Step 4. Divide the envolpe into subenvelopes.

The altitude interval is divided only at $M_{\min}$ to avoid divergence between the Mach and altitude directions. When the cumulative value of the gap metric reaches a threshold τ, expressed as

$$\sum\nolimits_{i=i_0}^{k} \delta_{gap}\left(P_{i,j}, P_{i+1,j}\right) \geq \tau, j = 1 \left(M = M_{\min}\right), \tag{9}$$

https://doi.org/10.1017/aer.2025.19 Published online by Cambridge University Press

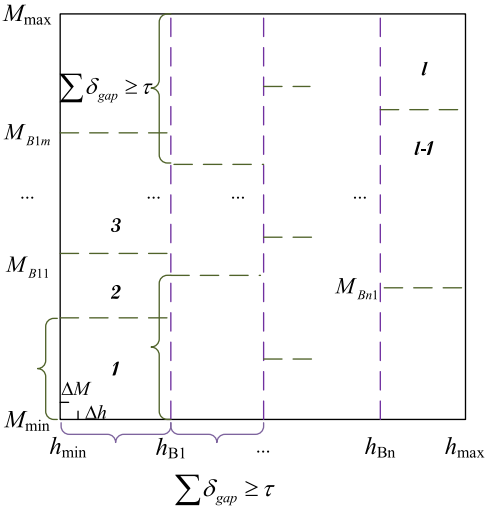


Figure 3. *Division of the envelope into subenvelopes.*

the corresponding interval numbers can be considered the altitude boundaries of the subenvelope to divide the entire envelope, denoted by the set h_B. Here, $h_B = \{h_{B1}, h_{B2}, \ldots, h_{Bn}\}$, where each h_{Bi} is a boundary value in the altitude direction. i_0 is the starting index for the summation, and k is the number of intervals required for the cumulative gap metric to reach the threshold τ. After reaching the threshold τ, the next accumulation starts at $i_0 = k + 1$.

The speed interval is then divided at the altitude boundaries in the set h_B. Similarly, if

$$\sum_{j=j_0}^{k} \delta_{gap}\left(P_{i,j}, P_{i,j+1}\right) \geq \tau, i \in \{i \,|i = 1, i\Delta h \in h_B\}, \tag{10}$$

the corresponding interval numbers can be considered the Mach boundaries. Here, j_0 is the starting index of the summation. After reaching the threshold τ, the next accumulation starts at $k + 1$. For each altitude boundary, the Mach values are divided into multiple intervals. They can be considered as the boundaries under the corresponding altitudes, denoted by the sets M_{B1},. . .,M_{Bn}. The subintervals are then numbered in ascending order of altitude and Mach. Thus, ϕ can be divided into L subenvelopes based on these boundaries, denoted as $\phi_l, l = 1, 2, \ldots, L$.

This process ensures a systematic division of the envelope ϕ into subenvelopes with multiple Mach intervals under each altitude boundary, thereby providing detailed and flexible segmentation, as shown in Fig. 3.

Step 5. Select nominal points.

The points within the subenvelope ϕ_l that is least different from the other point linear models, called the nominal point E_l, are calculated. Notably, the nominal points must satisfy Equation (11)

$$\bar{\delta}_{gap}(E_l) = \min_{a=1,2,\ldots,n_M \times n_h} \left\{ \frac{1}{n_M \times n_h} \left[\sum_{b=1, b\neq a}^{n_M \times n_h} \delta_{gap}(E_a, E_b) \right] \right\}, \tag{11}$$

where n_M and n_h are the numbers of state points in ϕ_l along the velocity and altitude dimensions, respectively, and a and b index all state points in the ϕ_l. E_a is set to the nominal point being considered, and E_b represents all other state points within the subenvelope, except the nominal point.

This ensures that the selected nominal point E_l best represents the subenvelope ϕ_l, resulting in an accurate LPV model.

Step 6. Obtain the LPV model of the aircraft by fitting the LTI system corresponding to the nominal points.

https://doi.org/10.1017/aer.2025.19 Published online by Cambridge University Press

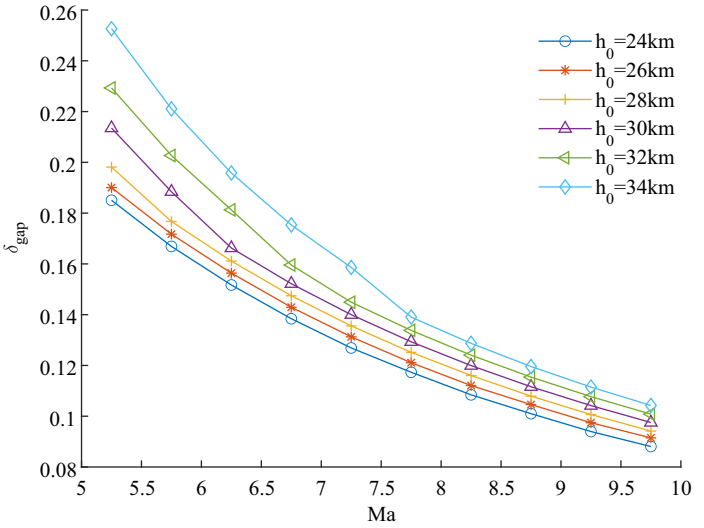


Figure 4. *Variation of gap metrics with Mach numbers at various altitudes.*

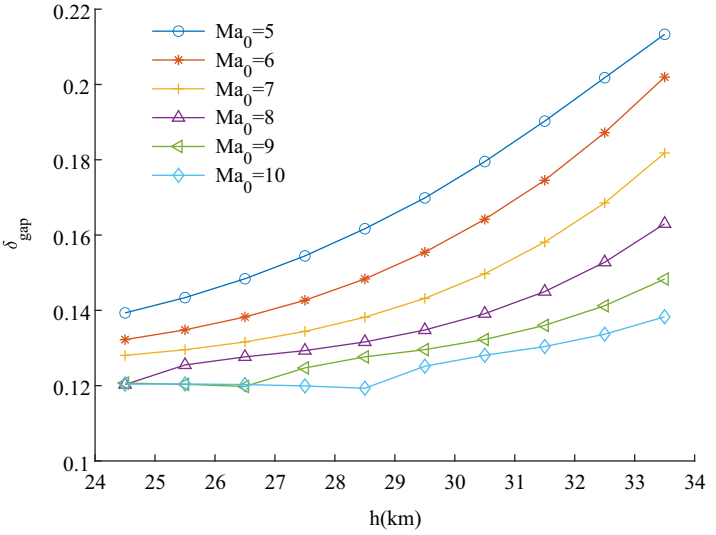


Figure 5. *Variation of gap metrics with altitudes at various Mach numbers.*

In this study, the NPS algorithm was used to derive the LPV model. This is achieved by linearising a set of LTI systems covering the region of interest, resulting in an LPV model that locally approximates the original nonlinear system around specific equilibrium points.

3.3 LPV model

The large flight envelope considered herein is $h = [24, 34]$ km, $M = [5, 10]$, which corresponds to a classic hypersonic flight envelope [38]. Using the algorithm proposed in section 3.2, we analysed the trend of the gap metrics under constant speed or altitude conditions. Figures 4 and 5 show the variation in the gap metrics with altitude and speed, respectively. As shown in Fig. 4, increasing the Mach number generally reduces the gap metric, indicating that the difference in model characteristics due to speed

https://doi.org/10.1017/aer.2025.19 Published online by Cambridge University Press

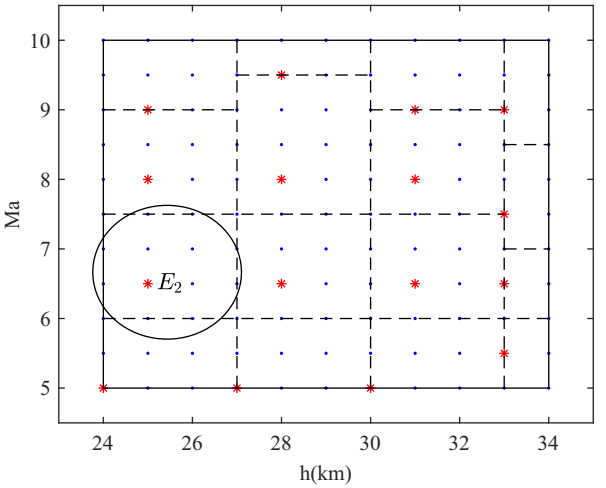


Figure 6. *Flight envelope division and schematic of the nominal points.*

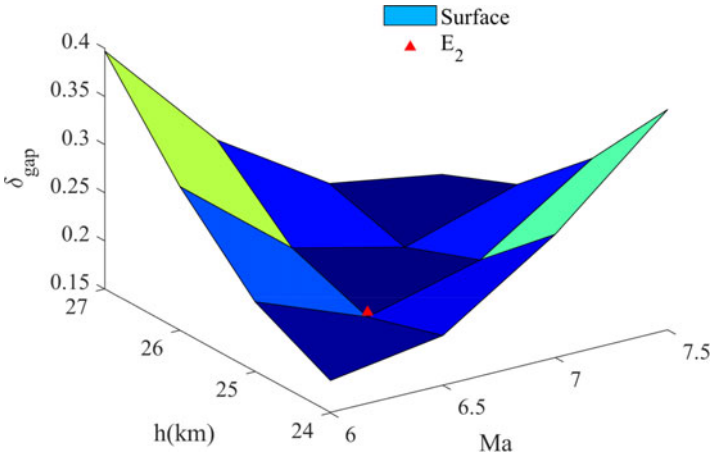


Figure 7. *Gap metric mean value of the second subenvelope.*

decreases with increasing speed, and this difference is more obvious at low altitudes. At different speeds, the trend of the clearance measures with altitude was similar, as shown in Fig. 5. With increasing altitude, the differences in the model characteristics due to the change in altitude increase, especially at lower Mach numbers. This indicates that the impact of altitude on the model characteristics is more pronounced at lower speeds.

Here, we consider $\Delta M = 0.5$, $\Delta h = 1$, and $\tau = 0.37$; thus, $N_{Ma} = N_h = 11$, which corresponds to 121 grid points. According to gap metric theory, the flight envelope is divided into 16 subenvelopes, and the nominal points of each subenvelope are calculated, as shown in Fig. 6. The blue and red points in the figure indicate the grid and nominal points, respectively. Taking the second sub-envelope as an example, the gap metrics between each state point and other state points are calculated, and the mean value is recorded (Fig. 7). Here, point E_2 ($h = 25$km, $M = 6.5$) has the smallest gap metric compared to the other state points, indicating that the model characteristics at point E_2 have the least variation from the rest of the points within the subenvelope. Therefore, the point with the minimal gap metric value E_2 can be selected as the nominal point.

https://doi.org/10.1017/aer.2025.19 Published online by Cambridge University Press

To simplify the range of values, the time-varying parameters M, h are normalised as follows:

$$\begin{cases} \delta_M = (2M - (M_{\max} + M_{\min})) \,/\, (M_{\max} - M_{\min}) \\ \delta_h = (2h - (h_{\max} + h_{\min})) \,/\, (h_{\max} - h_{\min}) \end{cases}, \tag{12}$$

where $\delta_M \in [-1, 1]$, $\delta_h \in [-1, 1]$.

Several LTI systems can be obtained by Jacobi linearisation at 16 equilibrium points in the flight envelope, and the LPV model is established by fitting them with δ_M and δ_h as the scheduling parameters:

$$\begin{cases} \dot{X} = A\left(\delta_M, \delta_h\right) X + B\left(\delta_M, \delta_h\right) U \\ Y = CX \end{cases}, \tag{13}$$

with $X = \left[v, \gamma, h, \alpha, q\right]^T$, $U = [\sigma, \delta_e]^T$,

$$A(v,h) = \begin{bmatrix} a_{11} & -\mu/r^2 & a_{13} & a_{14} & 0 \\ a_{21} & 0 & a_{23} & a_{24} & 0 \\ 0 & v & 0 & 0 & 0 \\ -a_{21} & 0 & a_{43} & a_{44} & 1 \\ a_{51} & 0 & a_{53} & a_{54} & a_{55} \end{bmatrix}, B(v,h) = \begin{bmatrix} b_{11} & 0 \\ b_{21} & 0 \\ 0 & 0 \\ b_{41} & 0 \\ 0 & b_{52} \end{bmatrix}, C = \begin{bmatrix} 1 & 0 & 0 & 0 & 0 \\ 0 & 1 & 0 & 0 & 0 \\ 0 & 0 & 1 & 0 & 0 \\ 0 & 0 & 0 & 1 & 0 \\ 0 & 0 & 0 & 0 & 1 \end{bmatrix},$$

where σ is the fuel equivalent ratio, δ_e is the elevator angle, and a_{11}, a_{13}, b_{11}, etc., are functions of δ_M and δ_h (see Appendix).

4.0 Adaptive gain scheduling of adrc with guardian map

4.1 Design of active disturbance rejection controller

Figure 8 shows the gain-scheduling framework, which comprises three key components: LADRC, LPV modeling based on gap metrics and gain scheduling using the GM. LADRC is central to vehicle attitude control, which is the core control method in this study. LPV models, which vary with vehicle altitude and speed, provide the foundation for calculating a stable region through the GM. The GM then dictates how control gains should be scheduled according to changes in altitude and speed, ensuring that the ADRC can meet the performance requirements of flight control.

The primary objective of this study is to control the attitude (angle-of-attack) of the aircraft. Therefore, an LPV model is extracted for the short-period mode, with only the elevator deflection angle δ_e as input and the angle-of-attack α and pitch rate q as state variables. Considering the control of the angle-of-attack, we designed an active disturbance rejection controller. According to the nonlinear model, the differential equation that describes the dynamics of α can be expressed as follows:

$$\begin{aligned} \ddot{\alpha} &= \dot{q} - \ddot{\gamma} = M/I_y - \ddot{\gamma} \\ &= 0.5\rho v^2 sc\left(C_{M\alpha} + C_{M\delta_e} + C_{Mq}\right)/I_y - \ddot{\gamma} \\ &= 0.5\rho v^2 sc \times 0.0292\delta_e/I_y + 0.5\rho v^2 sc\left(C_{M\alpha} + C_{Mq}\right)/I_y - \ddot{\gamma} \end{aligned} \tag{14}$$

Let $b_0 = 0.5\rho v^2 sc \times 0.0292/I_y$, $x_1 = \alpha$, $x_2 = \dot{\alpha}$. According to the total disturbance concept of active disturbance rejection control, let $f = 0.5\rho v^2 sc\left(C_{M\alpha} + C_{Mq}\right)/I_y - \ddot{\gamma}$ be the total disturbance, defined as the new state x_3.

Equation (14) can then be extended to the state-space form as follows:

$$\begin{cases} \dot{x}_1 = x_2 \\ \dot{x}_2 = x_3 + b_0\delta_e \\ \dot{x}_3 = \dot{f} \end{cases}. \tag{15}$$

https://doi.org/10.1017/aer.2025.19 Published online by Cambridge University Press

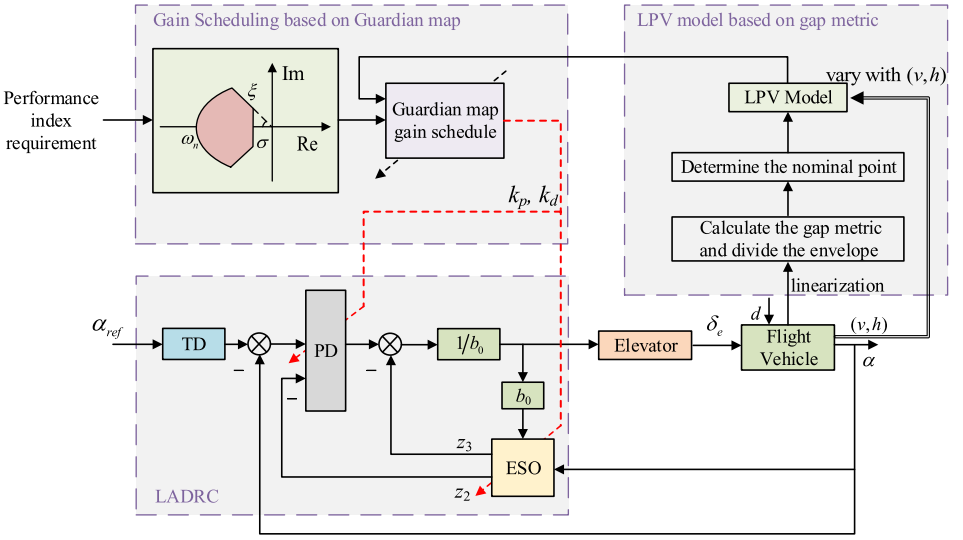


Figure 8. *Framework of the gain-scheduling control.*

Based on the idea of online disturbance compensation, the following extended state observer is designed to estimate the total disturbance in real time:

$$\begin{cases} \dot{z}_1 = z_2 + l_1 (x_1 - z_1) \\ \dot{z}_2 = z_3 + l_2 (x_1 - z_1) + b_0 \delta_e, \\ \dot{z}_3 = l_3 (x_1 - z_1) \end{cases} \tag{16}$$

where z_i $(i = 1, 2, 3)$ is the estimate of x_i $(i = 1, 2, 3)$, and $L = [l_1, l_2, l_3]^\intercal$ is the observer gain. To simplify the tuning process, the observer gains can be parameterised as $L = [l_1, l_2, l_3]^\intercal = \left[3\omega_o, 3{\omega_o}^2, {\omega_o}^3\right]^\intercal$ [17], where the observer bandwidth ω_o is the only tunable parameter.

The linear feedback control law is adopted as follows:

$$\delta_e = \frac{k_p \left(\alpha_{ref} - z_1\right) - k_d z_2 - z_3}{b_0}, \tag{17}$$

Thus, the closed-loop equation can be expressed as follows:

$$\begin{cases} \dot{X}_{cl} = A_{cl} (\delta_M, \delta_h) X_{cl} + B_{cl} (\delta_M, \delta_h) \alpha_{ref} \\ Y_{cl} = C_{cl} X_{cl} \end{cases} \tag{18}$$

with $X_c = \left[\alpha, q, z_1, z_2, z_3\right]^{\mathrm{T}}$,

$$A_{cl} (\delta_M, \delta_h) = \begin{bmatrix} a_{44} & 1 & 0 & 0 & 0 \\ a_{54} & a_{55} & -\frac{b_{52} k_p}{b_0} & -\frac{b_{52} k_d}{b_0} & -\frac{b_{52}}{b_0} \\ 3\omega_o & 0 & -3\omega_o & 1 & 0 \\ 3{\omega_o}^2 & 0 & -3{\omega_o}^2 - k_p & -k_d & 0 \\ {\omega_o}^3 & 0 & -{\omega_o}^3 & 0 & 0 \end{bmatrix}, B_{cl} (\delta_M, \delta_h) = \begin{bmatrix} 0 \\ \frac{b_{52} k_p}{b_0} \\ 0 \\ k_p \\ 0 \end{bmatrix},$$

https://doi.org/10.1017/aer.2025.19 Published online by Cambridge University Press

$$C_{cl}\left(\delta_M, \delta_h\right) = \begin{bmatrix} 1 & 0 & 0 & 0 & 0 \\ 0 & 1 & 0 & 0 & 0 \\ 0 & 0 & 1 & 0 & 0 \\ 0 & 0 & 0 & 1 & 0 \\ 0 & 0 & 0 & 0 & 1 \end{bmatrix}.$$

Next, we designed a suitable controller parameter gain-scheduling algorithm to tune k_p and k_d for different operating conditions.

4.2 Guardian map theory and stability analysis

Guardian maps are scalar maps that project a set of real matrices of order N onto a region of a complex plane. Let ν map $\mathrm{R}^{n\times n}$ onto the entire complex plane $\mathbb{C}$, and Ω is a known region in the complex plane. The stability sets of interest are as follows [27]:

$$S\left(\Omega\right) = \left\{A \in \mathrm{R}^{n\times n} : \lambda\left(A\right) \subset \Omega\right\}. \tag{19}$$

Definition 3. *Let ν map $R^{n\times n}$ onto $\mathbb{C}$. The map ν guards $S\left(\Omega\right)$ if the following equivalence holds for all $A \in \bar{S}\left(\Omega\right)$:*

$$\nu\left(A\right) = 0 \text{ if and only if } A \in \partial S\left(\Omega\right), \tag{20}$$

where $\bar{S}\left(\Omega\right)$ denotes the closure of the set $S\left(\Omega\right)$, and $\partial S\left(\Omega\right)$ is the boundary of $S\left(\Omega\right)$.

Figure 9 shows the GMs of some regions.

(1) Hurwitz stability ($\Omega = \mathbb{C}_-$): A GM is expressed as follows:

$$\nu_H\left(A\right) = \det\left(A \otimes I\right) \det\left(A\right). \tag{21}$$

where $\otimes$ denotes the bialternate product [27] (see Appendix). Stability margin: The open σ-shifted left half-plane region ($\mathrm{Re}\left(z\right) < \sigma$) is guarded by the following equation:

$$\nu_\sigma\left(A\right) = \det\left(A \otimes I - \sigma I \otimes I\right) \det\left(A - \sigma I\right). \tag{22}$$

The region enclosed by the circle centred at the origin of the complex plane with radius ω_n. A GM that corresponds to this conic damping ratio region is expressed as follows:

$$\nu_{\omega_n}\left(A\right) = \det\left(A \otimes A - {\omega_n}^2 I \otimes I\right) \cdot \det\left(A^2 - {\omega_n}^2 I\right). \tag{23}$$

A conic surface with an interior angle of 2γ, and a region with a damping ratio greater than $\xi = \cos\gamma$. The corresponding GMs are expressed as follows:

$$\nu_\xi\left(A\right) = \det\left(A^2 \otimes I + \left(1 - 2\xi^2\right) A \otimes A\right) \det A. \tag{24}$$

The GMs for the stabilisation region of the flight control system considering the stable margin, natural frequency and damp ratio are as follows:

$$\nu\left(A\right) = \nu_\sigma\left(A\right) \cdot \nu_\xi\left(A\right) \cdot \nu_{\omega_n}\left(A\right). \tag{25}$$

Based on these, a GM related to a specific region can be obtained. To analyse the largest variation range of the parameter that guarantees the stability of the parameterised matrices, we introduce Lemma 1 [27].

https://doi.org/10.1017/aer.2025.19 Published online by Cambridge University Press

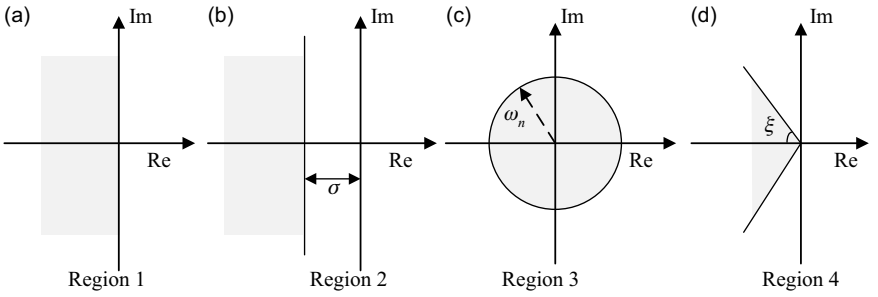


Figure 9. *Guardian maps (GMs) for some stable regions.*

Lemma 1. *When r is scalar and there is $r_{min} \le r \le r_{max}$, for some value of r_0 such that $A(r_0)$ is stable with respect to Ω, ν guards $S(\Omega)$. Therefore, the largest stable interval that stabilises $A(r)$ with respect to Ω and contains r_0 is $r \in [r^-, r^+]$, where*

$$\begin{cases} r^- = \sup\ \{r < r_0 : \nu_\Omega [A(r)] = 0\} \\ r^+ = \inf\ \{r > r_0 : \nu_\Omega [A(r)] = 0\} \end{cases} \tag{26}$$

r^- is the largest real root of $\nu_\Omega [A(r)] = 0$ on the interval $[r_{\min}, r_0)$ (if it does not exist, then $r^- = r_{\min}$), and r^+ is the smallest real root of $\nu_\Omega [A(r)] = 0$ on the interval $[r_0, r_{\max})$ (if it does not exist, then $r^+ = r_{\max}$).

When r is scalar, given a stable region Ω, the range of values of $A(r)$ with respect to the region stable r can be obtained from Lemma 1 using GMs ν.

We consider the stability of two-parameter polynomial families of real matrices (or polynomials) relative to a domain Ω for which $S(\Omega)$ is endowed with a polynomic GM ν_Ω

$$A(r_1, r_2) = \sum_{i=0}^{i=k} \sum_{j=0}^{j=l} r_1^i r_2^j A_{ij}, \tag{27}$$

where r_1 and r_2 are the real parameters. To analyse the necessary and sufficient conditions for the stability of $A(r_1, r_2)$ over a specific rectangle-shaped domain $(r_1, r_2) \in [\alpha_1, \beta_1] \times [\alpha_2, \beta_2]$ Lemma 2 [39] is introduced. The aim is to find the largest stable open rectangle with a fixed side. First, let $r^0 = (r_1^0, r_2^0)$ be a nominal parameter vector such that $A(r_1^0, r_2^0)$ is Ω stable. By freezing one of the parameters ($r_2 = r_2^0$), the largest (open) interval containing r_1^0, $I_{\max}(r_2^0) = (r_1^-, r_1^+)$ can be computed such that $\forall r_1 \in I_{\max}(r_1, r_2^0) \in S(\Omega)$ (Lemma 1). Let $\nu_1(r_2) = p_{[r_2]}(r_{1s}^-)\, p_{[r_2]}(r_{1s}^+)$, wherein $p_{[r_2]}(r_1) = \nu_\Omega [A(r_1, r_2)]$ represents a polynomial with r_1 as the variable for each r_2.

Lemma 2. *Let $A(r_1, r_2)$ be expressed as in Equation (27), where $r_{1,min} \le r_1 \le r_{1,max}$, $r_{2,min} \le r_2 \le r_{2,max}$. Let $A(r_1^0, r_2^0) \in S(\Omega)$ and let ν_Ω be a GM for $S(\Omega)$. We choose $[r_{1s}^-, r_{1s}^+] \subset I_{max}(r_2^0)$. We define $\underline{r}_2 = sup\{r_2 \in [r_{2,min}, r_2^0) : \nu_1(r_2) = 0\}$ $(or - \infty if none exist)$ and $\bar{r}_2 = inf\{r_2 \in (r_2^0, r_{2,max}] : \nu_1(r_2) = 0\}$ $(or + \infty if none exist)$. The largest stability domain containing $(r_1^-, r_1^+) \times r_2^0$ is then defined as $[r_{1s}^{-,+}] \times (\underline{r}_{-2}, \bar{r}_2)$.*

4.3 Controller parameter gain-scheduling algorithm based on GM

Parameter tuning based on GM is an offline tuning method that adjusts the control parameters by determining whether the closed-loop poles meet the performance requirements within the target region. The target region adopted herein is defined as Equation (25) in section 4.2, encompassing the constraints on the closed-loop poles residing in the left half of the complex plane.

https://doi.org/10.1017/aer.2025.19 Published online by Cambridge University Press

Gain scheduling under all operating conditions is a 2D scheduling problem that considers both altitude and Mach number. The basic concept is as follows: The traversal is performed over the envelope of the Mach number [5, 10] × [24, 34]km. A controller is first designed at the left boundary point of the domain ($M = 5$, $h = 24$km, i.e. $\delta_M = -1$, $\delta_h = -1$). Then, δ_h is fixed as -1, and Lemma 1 is employed to calculate the variable range for which the controller can stabilise the system. Next, new controller parameters are searched at the right boundary point of the stable range, and the corresponding stable variable range is calculated. This process is iterated until the stable variable range covers the entire Mach interval. Finally, Lemma 2 is employed to determine the maximum stable altitude region. The process is iterated at the upper bound of the altitude interval to generate a set of controller gains that ensure stability across the full operational envelope.

The procedure is as follows and is illustrated in detail in Algorithm 1.

Algorithm 1 Mach-altitude adaptive gain-scheduling algorithm based on GM

Step 1: Initialisation

(1) Define the target stabilisation region Ω_t and the corresponding GM ν_{Ω_t}.

(2) Specify the ranges of Mach numbers $\left(\delta_{M,\min}, \delta_{M,\max}\right)$, and altitudes $\left(\delta_{h,\min}, \delta_{h,\max}\right)$.

(3) Let $i = 1$, $\delta_h^i = \delta_{h,\min}$.

Step 2: Controller parameter initialisation

Fix δ_h^i. Let $j = 1$ and $\delta_{M0} = \delta_{M,\min}$. Find an initial controller parameter $K_j = \left[k_p, k_d\right]$ that ensures that the characteristic roots of $A\left(\delta_{M0}, \delta_{h0}, K_j\right)$ lie within Ω_t.

Step 3: Robustness analysis

(1) Calculate $\nu_{\Omega_t}\left[A\left(\delta_M, \delta_h^i, K_j\right)\right] = 0$ and use Lemma 1 to calculate the maximum interval $\left(\delta_{M,j}^-, \delta_{M,j}^+\right)$ for which $\nu_{\Omega_t}\left[A\left(\delta_M, \delta_h^i, K_j\right)\right]$ is stable with respect to Ω_t.

(2) If $\delta_{M,j}^+ \geqslant \delta_{M,\max}$, go to Step 6; otherwise, go to the next step with $\delta_{M,j} = \delta_{M,j}^+$.

Step 4: Find the central controller parameter K_{j+1}

The central value of the stable region is obtained iteratively using a 2D search algorithm to determine the central controller parameters K_{j+1}, which provide the maximum margin. The maximum search times and the termination accuracy are specified as N_s and ε, respectively.

(1) Let $\delta_{M,j} = \delta_{M,j}^+$, $m = 1$ and $K^m = K_j$.

(2) While $m < N_s$, fix k_d and use Lemma 1 to find the largest stability interval for k_p as $k^{m+1} = \left(k_p^{m-} + k_p^{m+}\right)/2$.

(3) Fix k_p and seek the largest stability interval for k_d as $k_d^{m+1} = \left(k_d^{m-} + k_d^{m+}\right)/2$.

(4) When $K^{m+1} - K^m \leq \varepsilon\left(1 + K^m\right)$, go to Step 5; otherwise, let $m = m + 1$ and go to Step 2.

(5) $K_{j+1} = K^{m+1}$. Recalculate the GM $\nu_{\Omega_t}\left[A\left(\delta_M, \delta_h, K_{j+1}\right)\right] = 0$ and seek the next stability interval $\left(\delta_{M,j+1}^-, \delta_{M,j+1}^+\right)$ containing $\delta_{M,j}$.

(6) If $\delta_{M,j+1}^+ \geqslant \delta_{M,\max}$, proceed to Step 5; otherwise, repeat Step 4 with $j = j + 1$.

Step 5: Determine the range of $\delta_h \begin{pmatrix} {}^{i}_{-h}\delta, {}^{-i}_{h}\delta \end{pmatrix}$ when K_j stablises $A\left(\delta_M, \delta_h^i, K_j\right)$ with respect to Ω_t

(1) Use Lemma 2 to find the largest stability domain $\left(\delta_{M,j}^-, \delta_{M,j}^+\right) \times \left(\underline{\delta}_{h,j}^i, \bar{\delta}_{h,j}^i\right)$ containing.

(2) Take their largest common intersection as $\begin{pmatrix} {}^{i}_{-h}\delta, {}^{-i}_{h}\delta \end{pmatrix}$.

Step 6: Terminating indicator

If $\bar{\delta}_h^i > \delta_{h,\max}$, the end. Otherwise let $\delta_h^{i+1} = \bar{\delta}_h^i$, $i = i + 1$, and return to Step 2.

This process generates a set of controller parameters $\left\{K_1, K_2, \ldots K_j\right\}$ and the corresponding range sets $\left\{\left[\delta_{M,\min}, \delta_{M,1}^+\right), \ldots, \left(\delta_{M,j}^-, \delta_{M,j}^+\right), \ldots, \left(\delta_{M,j}^-, \delta_{ma,\max}\right]\right\} \times \left(\underline{\delta}_h^i, \bar{\delta}_h^i\right)$ that meet the stability requirements.

https://doi.org/10.1017/aer.2025.19 Published online by Cambridge University Press

Table 2. *The parameters in the simulation*

Parameters	Values	Parameters	Values
N_h	5	ε	0.01
N_s	20	ω_o	15
$\delta_{M,\min}$	-1	$\delta_{h,\min}$	-1
$\delta_{M,\max}$	1	$\delta_{h,\min}$	1

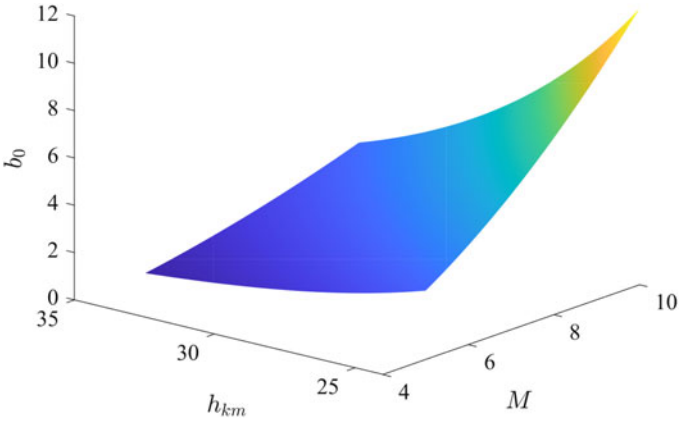


Figure 10. *Variation of control efficiency within the flight envelope.*

An analytical expression for the controller parameters K as a function of the variable (δ_M,δ_h) can be derived by curve fitting.

Remark: Assuming the length of each side of a rectangle is constrained to be less than the Lipschitz constant L, it is guaranteed that smaller rectangles can adequately cover the entire envelope.

5.0 Results and discussions

The simulation parameters are listed in Table 2. The controller design criteria consider the stability margin, the short-period damping ratio and the natural frequency. To ensure good stationarity, rapidity and high precision, the constraints of assigning the closed-loop pole in the target stability region are a stability margin $|\sigma| \geqslant 4$ and a damping ratio $\xi \geqslant 0.707$, and a natural frequency $\omega_n \leq 16$.

Figure 10 shows the variation in the control efficiency within the flight envelope. The control efficiency increased from approximately 2 to 12, highlighting the necessity of gain-scheduled control. As shown in Fig. 11 when $\delta_h = 1$, there is almost no intersection in the case of $\delta_M = -1$ and $\delta_M = 1$, indicating that a single controller cannot meet all the conditions. These results demonstrate that the gain-scheduling controller is vital.

The algorithm described in section 4.3 was employed to calculate gain scheduling with Mach and altitude. First, the initial controller K_1 at the starting point ($M = 5$, $h = 24$km, i.e. $\delta_M = -1$, $\delta_h = -1$) was designed to ensure that the closed-loop poles were within the target region. According to Lemma 1, K_1 can cover a Mach number range of $(-1.489, 0.022)$. With δ_M fixed at the right boundary point 0.022, the 2D search algorithm obtains the centre value of the stable region as the new controller K_2 (Fig. 12). Algorithm 1 was applied and iterated to obtain the values of 49 groups of controllers (see Table A1 in the Appendix for details). The 49 groups of controllers can cover all the conditions. k_p and k_d can be obtained by fitting δ_M and δ_h as variables in Equation (28), as shown in Fig. 13.

https://doi.org/10.1017/aer.2025.19 Published online by Cambridge University Press

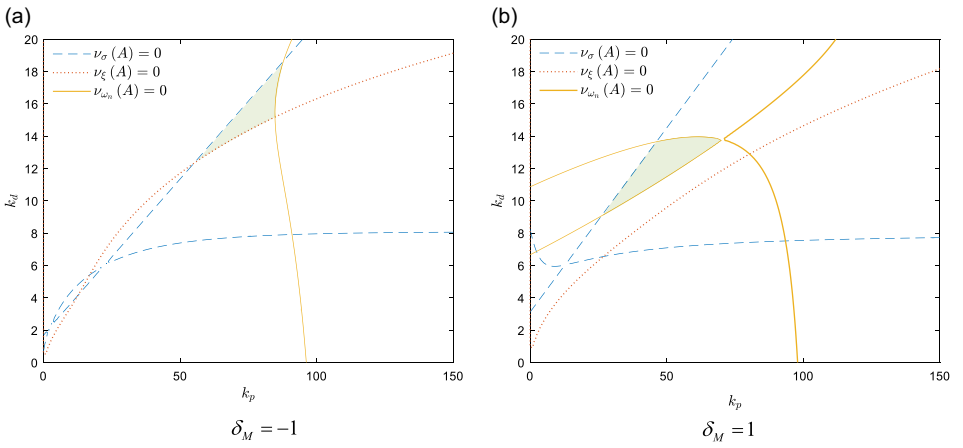


Figure 11. *Stabilising gain regions for different values of* $\delta_M = \{1, -1\}$ *when* $\delta_h = 1$.

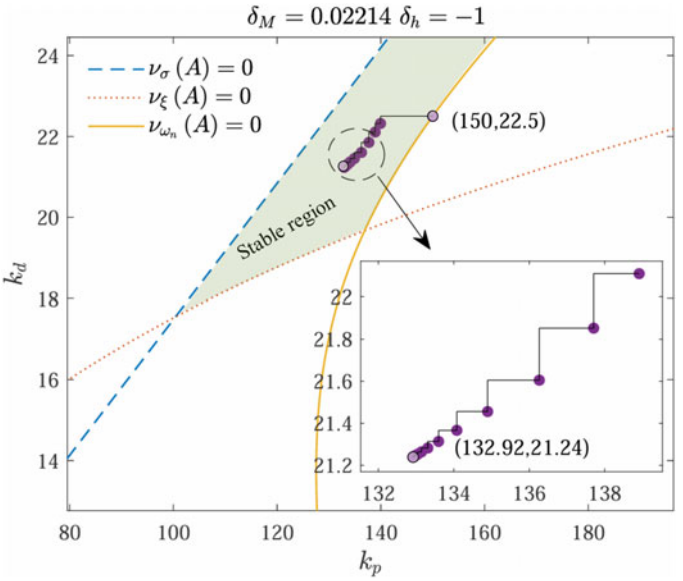


Figure 12. *Procedure for seeking primary and central controllers in a 2D subspace.*

$$\begin{cases} k_p = 1.414\delta_M^2 + \ 2.058\delta_h^2 - 1.133\delta_M\delta_h - 4.08\delta_M - 2.592\delta_h + 16.92 \\ k_d = 8.133\delta_M^2 - 3.538\delta_h^2 + 1.454\delta_M\delta_h - 23.89\delta_M - 27.01\delta_h + 101.8 \end{cases} \tag{28}$$

For the intervals of $\delta_M \in [-1, 1]$, $\delta_h \in [-1, 1]$, values were taken every 0.2, resulting in a total of 121 state points. Under different Mach and flight altitudes, the control law Equation (28) was applied to the closed-loop state Equation (18). Figure 14 shows the pole distributions of the short-period modes corresponding to the short-period modes under the given conditions. The open-loop poles have a low damping ratio and are close to the imaginary axis, whereas the closed-loop poles are in the target region, which satisfies the flight control performance index.

https://doi.org/10.1017/aer.2025.19 Published online by Cambridge University Press

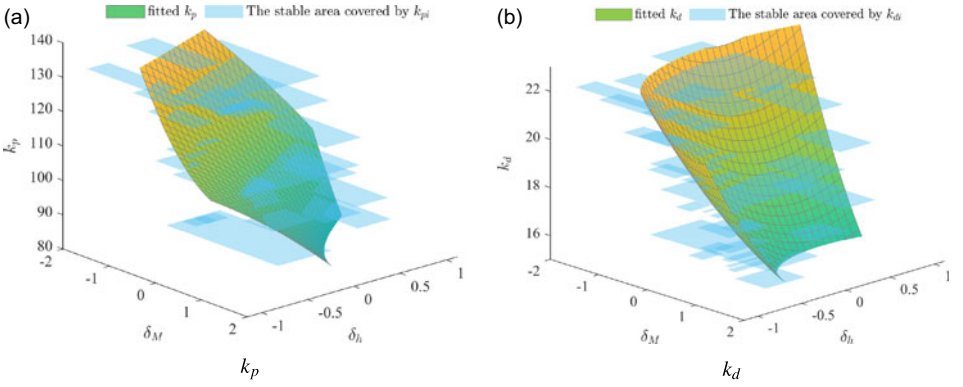


Figure 13. *Variation of the controller parameters k_p and k_d with δ_M and δ_h.*

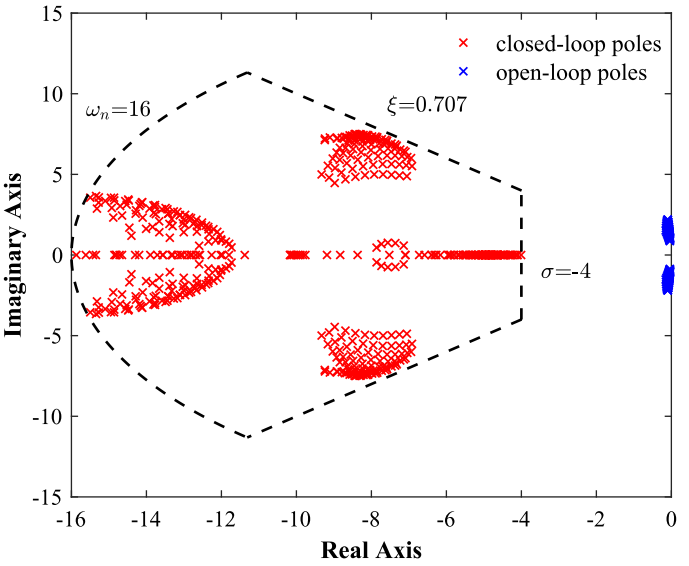


Figure 14. *Open and closed-loop pole distributions for the full flight envelope.*

5.1 Simulation of step response and climb phase

To verify the effectiveness of the proposed method, we compared it with the traditional ADRC method and GM-LQR developed by Xiao et al. [30]. The proposed gain-scheduling algorithm based on GM is called 'GM-ADRC', and that applied to the PID control is termed 'GM-PID'. The traditional ADRC algorithm (hereafter ADRC) does not perform gain scheduling of k_p and k_d but only adjusts the corresponding b_0 according to different working conditions. The gain value of ADRC was taken from a point $[k_p,k_d] = [102.38, 17.84]$ of the fitted surface.

Test 1: Step response test under all conditions

Given a step signal with an amplitude of 3° as the angle-of-attack tracking command signal, the angle-of-attack response curve is shown in Fig. 15. The integral of the time absolute error (ITAE), integral of the absolute error (IAE), and settling time (T_s) were employed as performance indicators to compare the results of the algorithms (Table 3).

Both GM-ADRC and ADRC could quickly follow the given value, demonstrating good response characteristics and indicating the feasibility of ADRC control. The GM-ADRC was faster than the standard

https://doi.org/10.1017/aer.2025.19 Published online by Cambridge University Press

Table 3. *Performance index comparison of Experiment 1*

	Two-parameter scheduling control		
Controllers	ITAE	IAE	Ts
GM-ADRC	0.3016	1.0324	0.8395
ADRC	0.3063	1.0685	0.8635

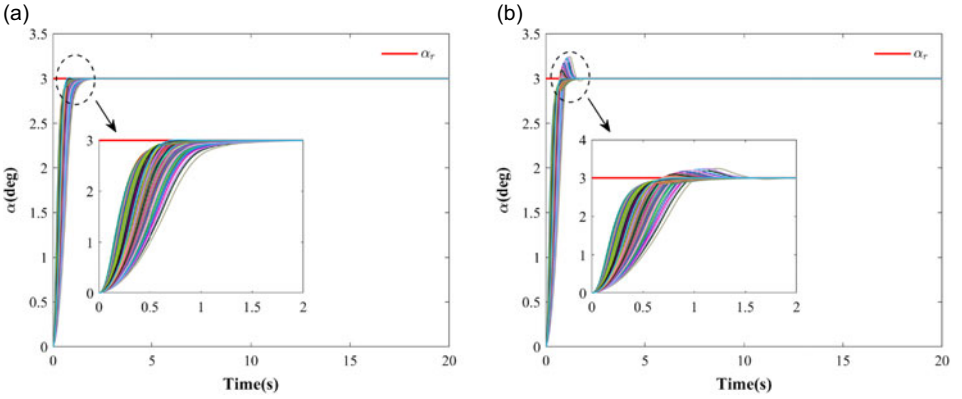


Figure 15. *α response under different operating conditions.*

ADRC and exhibited superior performance indicators. GM-ADRC exhibited a lower ITAE than ADRC, indicating that it not only responded faster but also had a lower overall error over time. The lower IAE value for GM-ADRC also indicates that the magnitude of the cumulative error throughout the response is reduced. Finally, the lower T_s value for GM-ADRC confirms that the algorithm reaches the desired output level sooner, indicating that the proposed algorithm exhibited faster adjustment to changes and disturbances.

Figures 16 and 17 show the response curves of the pitch angle rate q and the elevator deflection angle δ_e at different Mach numbers, respectively. δ_e and q are stabilised, and q is also stabilised at approximately 0 (deg/s), indicating that the vehicle finally maintains a stable attitude. Therefore, the proposed controller exhibits a good control effect.

Test 2: Gain-scheduling control in the power climb stage

To verify the effectiveness of the algorithm in trajectory flight, we designed guidance instructions and employed the proposed gain-scheduling control in the powered climb stage. In this phase, the climbing plus and constant altitude cruise flight state should be achieved. The guidance instruction for the angle-of-attack was obtained by PID control of the actual altitude error, which is used as the tracking instruction signal for the actual attitude control. The altitude guidance instructions are as follows:

$$h_r = \begin{cases} -at^2 + h_0, 0 < t \le t_1 \\ -2at_1 t + b, t_1 < t \le t_2 \\ a\left(t - t_f\right)^2 + h_c, t_2 < t \le t_f \\ h_c, t > t_f \end{cases}, \tag{29}$$

where $a = \frac{h_0 - h_c}{\left(t_f - t_m\right)t_m + \left(t_f - t_m\right)^2/2}$, $b = a\left(t_f - t_m\right)^2/4 + h_0$, $t_m = t_2 - t_1$.

https://doi.org/10.1017/aer.2025.19 Published online by Cambridge University Press

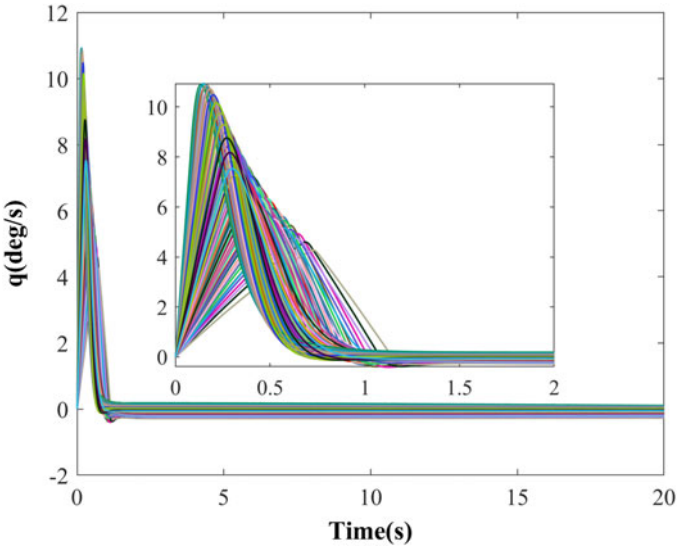


Figure 16. *qresponse under different operating conditions.*

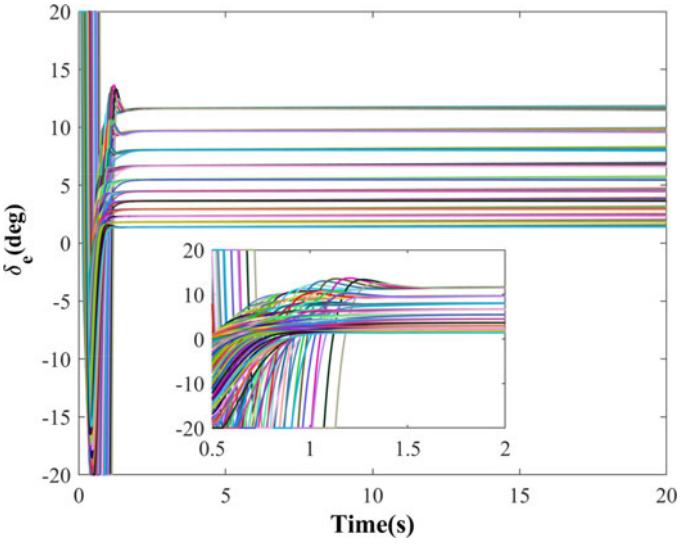


Figure 17. *$\delta_e$response under different operating conditions.*

The angle-of-attack guidance instructions are as follows:

$$\alpha_r = \begin{cases} k_{ph}\text{sat}\,(\Delta y, 500) + k_{dh}\Delta\dot{y} + \alpha_0, 0 < t \le t_{y=500} \\ k_{ph}\text{sat}\,(\Delta y, 500) + k_{dh}\Delta\dot{y} + k_{ih}\int_{t_{y=500}}^{t} \Delta y dt, t > t_{y=500} \end{cases},$$

with $\text{sat}\,(\Delta h, 500) = \begin{cases} \Delta h, |\Delta h| \le 500 \\ 500, \Delta h > 500 \\ -500, \Delta h < -500 \end{cases}$, $\Delta h = h_r - h$ is the height error, $t_{h=500}$ is the first time Δh=500m, and $\Delta\dot{h}$ is the derivative of the height error.

The above angle-of-attack of the guidance command was adopted, and the parameters were set as follows: $t_1 = 150$, $t_2 = 250$, $t_f = 400$, $h_0 = 22$km, $h_c = 33.5$km, $k_{ph} = 0.0074$, $k_{dh} = 0.0573$, and

https://doi.org/10.1017/aer.2025.19 Published online by Cambridge University Press

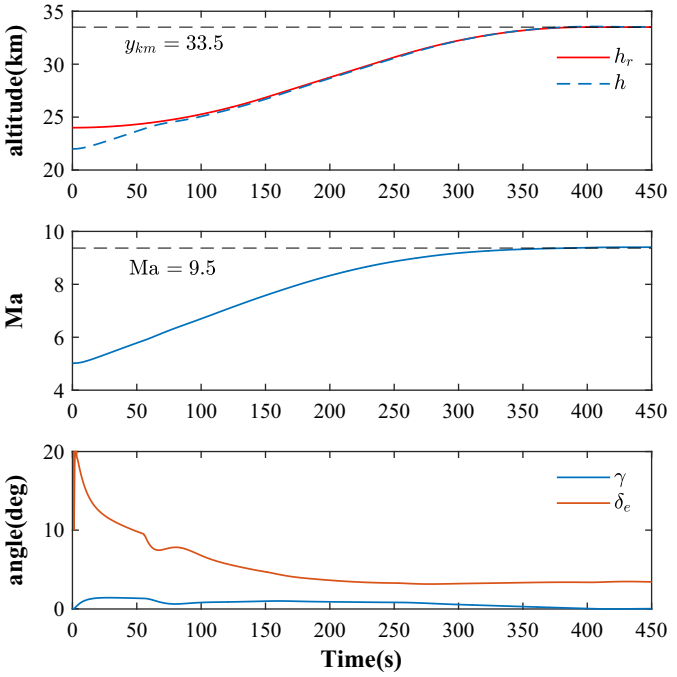


Figure 18. *Variation of altitude, δ_e, and γ with time.*

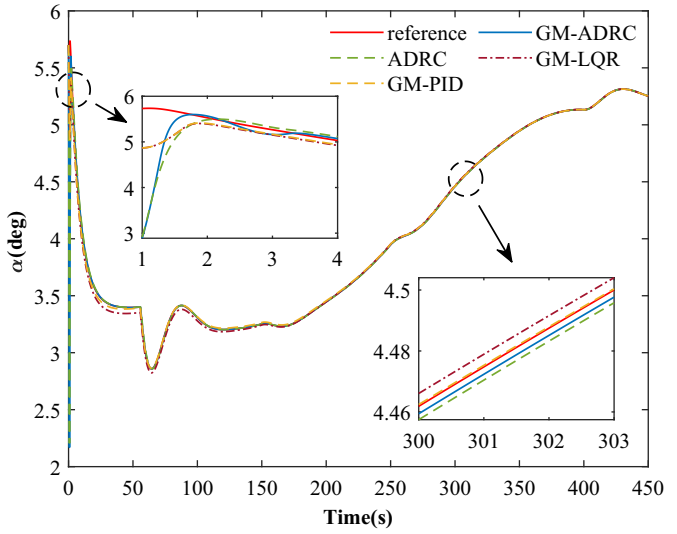


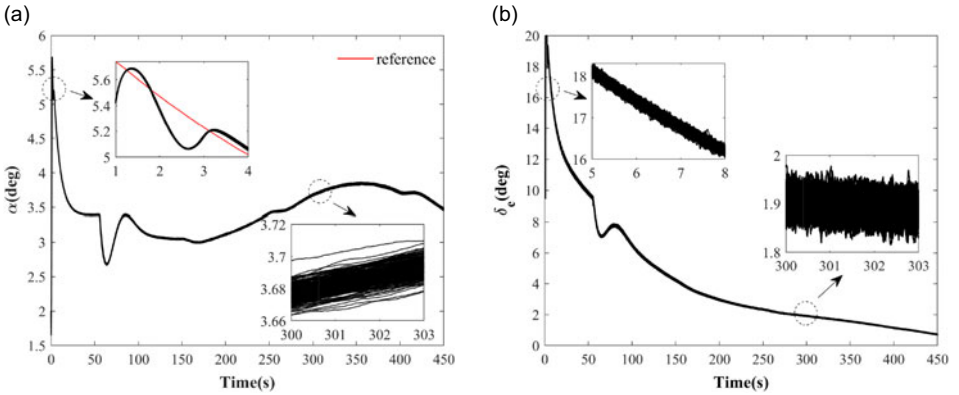
Figure 19. *Comparison of the angle-of-attack α tracking for the different algorigthms.*

$k_{ih} = 1.146 \times 10^{-4}$. Figure 18 shows the obtained altitude and velocity of the particle trajectory along with the corresponding state variables. The results show that the proposed gain-scheduling strategy can be employed in the climbing stage of aircraft. Furthermore, we compared the angle-of-attack tracking effects and performance indicators of GM-ADRC, ADRC, GM-PID and GM-LQR [30] (Fig. 19 and Table 4). All algorithms could follow the angle-of-attack instructions, but GM-ADRC exhibited the lowest ITAE (2.0329) and IAE (0.0621), indicating better tracking accuracy.

https://doi.org/10.1017/aer.2025.19 Published online by Cambridge University Press

Table 4. *Performance index comparison of Experiment 2*

	Gain scheduling control in the power climb stage	
Controllers	ITAE	IAE
GM-ADRC	2.0329	0.0621
ADRC	4.4902	0.0975
GM-PID	5.9912	0.0811
GM-LQR [30]	22.1278	0.2491



α δ_e

Figure 20. *Change curve of α and δ_e with 20% aerodynamic parameters bias.*

5.2 Robustness analysis

To account for uncertainties in the vehicle model, random variations of up to 20% were introduced to each aerodynamic parameter, and Monte Carlo simulations were performed 1,000 times to evaluate the robustness of the control system. Monte Carlo simulations were performed 1,000 times to evaluate the robustness of the control system. Figure 20 shows the angle-of-attack α and elevator deflection δ_e curves of the proposed algorithm. The results demonstrate that within the specified uncertainty range, the angle-of-attack consistently follows the commanded signal, and the controller exhibits robust and reliable performance in maintaining control effectiveness.

To evaluate the aircraft's response to wind gusts, we simulated the climb phase under gust disturbance. The Horizontal Wind Model (HWM) [40,41], which is widely recognised and adopted by the U.S. Department of Defense [42], was employed to mathematically represent continuous gusts. This model characterises the horizontal wind field in the stratosphere based on changes in altitude and latitude. The tangential wind velocity is expressed as follows:

$$v_{\text{wind}}(h,\varphi) = v_0(\varphi) + a(\varphi)(h-h_0) + b(\varphi)(h-h_0)^2, \tag{30}$$

where v_{wind} is the tangential wind speed at altitude h and latitude φ, h_0 is the reference altitude (set to 24 km herein), and φ was set to 45°. The baseline wind speed, $v_0(\varphi)$, is defined as $10 + 20 \cdot |\sin(\varphi \cdot \pi/180)|$. The coefficients $a(\varphi)$ and $b(\varphi)$, which represent the linear and quadratic altitude variations, are defined as $a(\varphi) = 2 + 0.1 \cdot |\sin(\varphi \cdot \pi/180)|$ and $b(\varphi) = 0.05 \cdot \cos(\varphi \cdot \pi/180)$, respectively.

Figure 21 shows the tangential wind speed profile. The wind disturbance was applied between 100 and 200s to evaluate the system's robustness under realistic atmospheric conditions. Figure 22 shows the angle-of-attack α response. The wind caused an initial sharp deviation in the angle-of-attack α response, but it gradually stabilised with a minor error. As shown in Table 5, the ITAE and IAE values demonstrate

https://doi.org/10.1017/aer.2025.19 Published online by Cambridge University Press

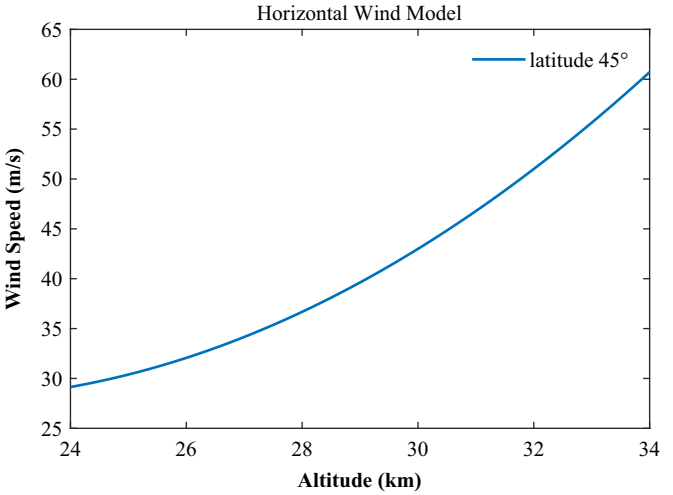


Figure 21. *Wind gust velocity profile.*

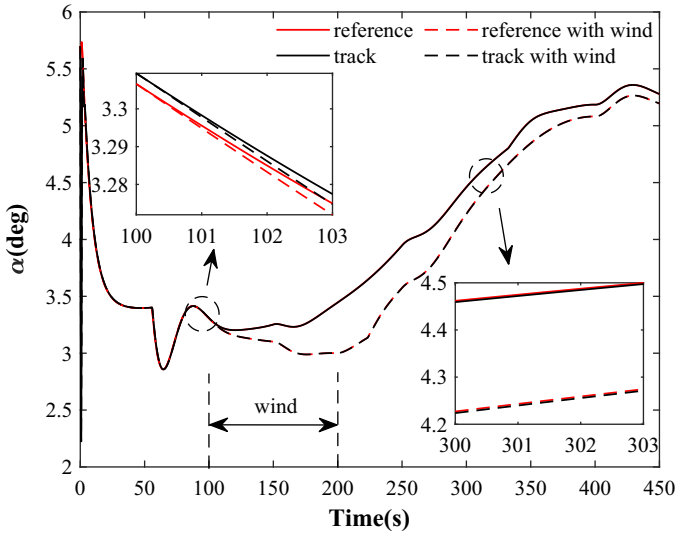


Figure 22. *Angle-of-attack (α) response under wind gust disturbance.*

the robustness and accuracy of the proposed controller compared with the GM-PID controller, particularly under wind disturbance. Figure 23 compares Mach-altitude flight envelopes with and without wind disturbance. Overall, the system maintained stability and consistency under disturbances, demonstrating its robustness and reliability in overcoming wind disturbances.

6.0 Conclusions

In this study, we developed an automatic gain-scheduling algorithm based on the GM theory using a more effective LPV model of aircraft as the object. The application of LADRC to a hypersonic vehicle leverages the advantages of traditional PID control, and it exhibits good control performance under severe model uncertainties. The proposed controller parameter gain-scheduling algorithm based on GMs eliminates the need to design a controller at multiple state points. This approach reduces the workload and streamlines the design process. The proposed algorithm meets the performance requirements of the

https://doi.org/10.1017/aer.2025.19 Published online by Cambridge University Press

Table 5. *Performance index comparison under wind disturbance*

	Tracking performance index	
Controllers	ITAE	IAE
GM-ADRC	2.0329	0.0621
GM-ADRC with wind	3.4785	0.0819
GM-PID	5.9912	0.0811
GM-PID with wind	11.3386	0.1094

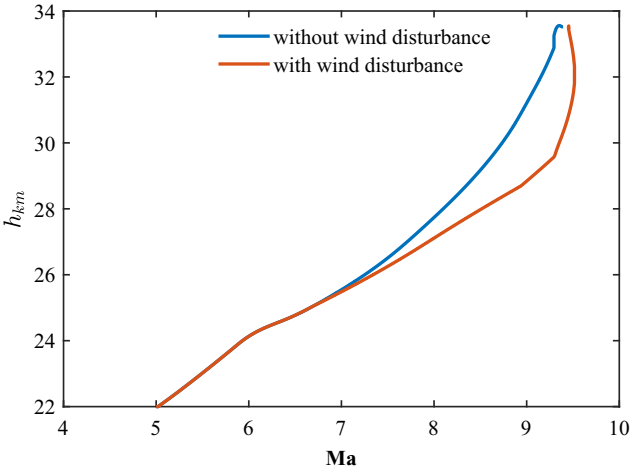


Figure 23. *Effects of wind disturbance on flight envelopes.*

entire envelope and outperforms the traditional ADRC, GM-PID and GM-LQR algorithms. To validate the robustness of the proposed algorithm, we performed Monte Carlo simulations of the aerodynamic parameters under wind disturbance.

Acknowledgements. This work was funded by the National Nature Science Foundation of China, Grant Nos. 62473209, 62073177 and 61973175. This manuscript builds upon the authors' prior conference paper, 'Active Disturbance Rejection Gain-Scheduling Control of Hypersonic Vehicle Based on Guardian Maps,' presented at the 2024 IEEE 13th Data-Driven Control and Learning Systems Conference (DDCLS), with several remarkable improvements and extensions.

Competing interests. The authors declare no competing interests relevant to the content of this article.

Ethical approval. This study is related to the improvement and application innovation of gain-scheduling algorithms; thus, it does not involve ethical issues. All authors are aware of this paper and agree to its submission.

Research transparency. No datasets were analysed during this study. The data generated in this study are available from the corresponding author upon reasonable request.

References

[1] Shahzad, S.K. and Hu, W.D. Hypersonic reentry trajectory planning by using hybrid fractional-order particle swarm optimization and gravitational search algorithm, *Chin J Aeronaut*, 2021, **34**, (1), pp 50–67.

[2] Mimouni, M.Z., Araar, O., Oudda, A. and Haddad, M. A new control scheme for an aerodynamic-surface-free tilt-rotor convertible UAV, *Aeronaut J*, 2024, **128**, (1324), pp 1119–1144.

[3] Wang, X. and Xu, B. Robust adaptive control of hypersonic flight vehicle with aero-servo-elastic effect, *IEEE Trans Aerosp Electron Syst* 2023, **59**, (2), pp 1955–1964.

[4] Suicmez, E.C. and Kutay, A.T. Full envelope nonlinear flight controller design for a novel electric VTOL (eVTOL), *Aeronaut J*, 2024, **128**, (1323), pp 966–993.

[5] Feng, Y., Sun, Z.H., Wu, L.N., Wang Y.S. and Xi, B. Nonlinear adaptive flight control system: performance enhancement and validation, *Chin J Aeronaut*, 2023, **36**, (4), pp 354–365.

https://doi.org/10.1017/aer.2025.19 Published online by Cambridge University Press

[6] Wang, G. and Xia, H.W. Fault-tolerant learning control of air-breathing hypersonic vehicles with uncertain parameters and actuator faults, *Expert Syst Appl*, 2024, **238**, p 121874.
[7] Ni, Z. and Fang, S. Study of the spike-aerodisk-opposing jet on heat protection to both the spike-aerodisk and the blunt body and overall drag reduction in rarefied hypersonic flow in near space, *Aerosp Sci Technol*, 2024, **147**, p109061.
[8] Qu, F., Wang, T., Liu, C., Fu, J. and Bai, J. Aerodynamic shape optimization of the vortex-shock integrated waverider over a wide speed range, *Aerosp Sci Technol*, 2023, **143**, p 108696.
[9] Wu, X., Zhou, Z. and Wang, Z.P. Rapid dynamic aeroelastic response analysis of the highly flexible wing with distributed propellers influence, *Aeronaut J*, Published online 2024, pp 1–23.
[10] Wang, F., Fan, P., Zhang, J., Fan, Y. and Yan, J. Preventing inlet unstart in air-breathing hypersonic vehicles using adaptive backstepping control with state constraints, *Acta Astronaut*, 2023, **211**, pp 498–509.
[11] Guo, L., Pang, L., Yang X, Zhao J and Ma, D. A power and thermal management system for long endurance hypersonic vehicle, *Chin J Aeronaut*, 2023, **36**, pp 29–40.
[12] Li N, Liu Y, Gong G, Zhao L, Yuan H. A generative deep learning approach for real-time prediction of hypersonic vehicles in fluid-thermo-structural coupling fields, *Aerosp Sci Technol*, 2023, **139**, p 108398.
[13] Xu, B. and Shi, Z. An overview on flight dynamics and control approaches for hypersonic vehicles, *Sci China Inf Sci*, 2015, **58**, (7), pp 1–19.
[14] Xu, B., Shou, Y., Shi, Z. and Yan, T. Predefined-time hierarchical coordinated neural control for hypersonic reentry vehicle, *IEEE Trans. Neural. Netw. Learning Syst.*, 2023, **34**, pp 8456–8466.
[15] Han, J. Auto-disturbances-rejection controller and its applications. *Control Decis*, 1998, **13**, (1), pp 19–23.
[16] Sun, M., Wang, Z. and Chen, Z. Practical solution to attitude control within wide envelope, *Aircr Eng Aerosp Tech*, 2014, **86**, (2), pp 117–28.
[17] Gao, Z. Scaling and bandwidth-parameterization based controller tuning, *American Control Conference*, 2003, vol. **4**, pp 4989–4996.
[18] Huang, Y. and Xue, W. Active disturbance rejection control: Methodology and theoretical analysis, *ISA Trans*, 2014, **53**, (4), pp 963–976.
[19] Xie, X., Wei, C., Gu, Z. and Shi, K. Relaxed resilient fuzzy stabilization of discrete-time Takagi–Sugeno systems via a higher order time-variant balanced matrix method, *IEEE Trans Fuzzy Syst*, 2022, **30**, pp 5044–5050.
[20] Ducard, G.J. and Allenspach, M. Review of designs and flight control techniques of hybrid and convertible VTOL UAVs, *Aerosp Sci Technol*, 2021, **118**, p 107035.
[21] Caigny, D., Camino, J.F., Oliveira, R., Peres, P. and Swevers, J. Gain-scheduled dynamic output feedback control for discrete-time LPV systems, *Intl J Robust & Nonlinear*, 2012, **22**, (5), pp 535–558.
[22] Kazemi, M.H. and Tarighi, R. PID-based attitude control of quadrotor using robust pole assignment and LPV modeling, *Int. J. Dynam. Control*, 2024, pp 1–13.
[23] Souza, L., Peixoto, M. and Palhares, R.M. New gain-scheduling control conditions for time-varying delayed LPV systems, *J Franklin Inst*, 2022, **359**, pp 719–742.
[24] Jiang, W., Zheng, C., Sun, X. and Wang, Y. Switching polytopic linear parameter-varying control for hypersonic vehicles in full envelope, *Int. J. Control Autom. Syst.*, 2023, **22**, pp 785–796.
[25] Jiang, W., Wu, K., Wang, Z. and Wang, Y. Gain-scheduled control for morphing aircraft via switching polytopic linear parameter-varying systems, *Aerosp Sci Technol*, 2020, **107**, p 106242.
[26] Vinco, G.M., Sename, O., Strub, G. Linear parameter-varying polytopic modeling and control design for guided projectiles, *J Guid Control Dynam*, 2024, **47**, (3), pp 433–447.
[27] Saydy, L., Tits, A. and Abed, E. Guardian maps and the generalized stability of parametrized families of matrices and polynomials, *Math Control Sig Syst*, 1990, **3**, (4), pp 345–371.
[28] Saussie, D., Ouassima, A. and Saydy, L. Aircraft pitch rate control design with guardian maps, *18th Mediterranean Conference on Control and Automation, MED'10*; Marrakech, Morocco; 2010, pp 1473–1478.
[29] Xiao, D., Liu, M., Liu, Y. and Lu, Y. Switching control of a hypersonic vehicle based on guardian maps, *Acta Astronaut*, 2016, **122**, pp 294–306.
[30] Liu, Y., Chen, B., Chen, J. and Liu, Y. Rapid parametric modeling and robust analysis for the hypersonic ascent based on gap metrics, *Appl Sci*, 2023, **13**, p 5189.
[31] Chen, B., Chen, J. and Liu, Y. Guardian maps based robust stability analysis with applications in flight control of hypersonic vehicles, *Aerosp Sci Technol*, 2020, **106**, p 106208.
[32] Cao, R., Wan, H.W., He, Z. and Lu, Y.P. Multiple model predictive control of perching maneuver based on guardian maps, *Chin J Aeronaut*, 2022, **35**, (5), pp 347–360.
[33] French, M. Adaptive control and robustness in the gap metric, *IEEE Trans Automat Contr*, 2008, **53**, pp 461–478.
[34] Shaughnessy, J.D., Pinckney, S.Z. and McMinn, J.D. Hypersonic vehicle simulation model: winged-cone configuration, NASA TM 102610, 1990.
[35] Marrison, C. and Stengel, R. Design of robust control systems for a hypersonic aircraft, *J Guid Control Dynam*, 1998, **21**, (1), pp 58–63.
[36] Tao, X., Li, N. and Li, S. Multiple model predictive control for large envelope flight of hypersonic vehicle systems, *Inform Sci*, 2016, **328**, pp 115–126.
[37] Cavanini, L., Ippoliti, G. and Camacho, E. Model predictive control for a linear parameter varying model of an UAV, *J Intell Robot Syst*, 2021, **101**, pp 1–18.
[38] Gao, H., Chen, Z., Sun, M., Huang, J, Wang, Z. and Chen, Z. An efficient fast altitude control for hypersonic vehicle, *Control Eng Pract*, 2020, **100**, p 104426.

https://doi.org/10.1017/aer.2025.19 Published online by Cambridge University Press

[39] Saussié, D., Saydy, L., Akhrif, O. and Berard, C. Gain scheduling with guardian maps for longitudinal flight control, *J Guid Control Dynam*, 2011, **34**, (4), pp 1045–1059.
[40] Drob, D.P., Emmert, J.T., Meriwether, J.W., Makela, J.J., Doornbos, E., Conde, M., and Klenzing, J.H. An update to the Horizontal Wind Model (HWM): The quiet time thermosphere, *Earth Space Sci*, 2015, **2**, (7), pp 301–319.
[41] Drob, D.P., Emmert, J.T., Crowley, G., Picone, J., Shepherd, G.G., Skinner, W., and Vincent, R.A. An empirical model of the Earth's horizontal wind fields: HWM07. *J Geophys Res Space Phys*, 2008, **113**, (A12).
[42] Madden, M.M. Verifying Implementation of the Dryden Turbulence Model and MIL-F-8785 Gust Gradient, 2018 *Modeling and Simulation Technologies Conference*, 2018, p 3580.

Appendix

The coefficient expression used in this paper is as follows:

$$a_{44} = -0.0509 + 0.02385\delta_h - 0.003929\delta_M - 0.01184\delta_h^2 + 0.01156\delta_h\delta_M + 0.001424\delta_M^2 + 0.008537\delta_h^3 - 0.00458\delta_h^2\delta_M - 0.002714\delta_h\delta_M^2 - 0.004934\delta_M^3.$$

$$a_{54} = -2.189 + 1.503_h + 0.5944\delta_M - 0.4935\delta_h^2 - 0.5536\delta_h\delta_M + 0.5009\delta_M^2 + 0.1115\delta_h^3 + 0.1955\delta_h^2\delta_M - 0.273\delta_h\delta_M^2 - 0.1359\delta_M^3.$$

$$a_{55} = -0.07845 + 0.04364\delta_h - 0.01365\delta_M - 0.0193\delta_h^2 + 0.02095\delta_h\delta_M - 0.004035\delta_M^2 + 0.004008\delta_h^3 - 0.004302\delta_h^2\delta_M - 0.003277\delta_h\delta_M^2 + 0.002232\delta_M^3.$$

$$b_{52} = 2.98 - 1.963\delta_h + 1.995\delta_M + 0.7185\delta_h^2 - 1.386\delta_h\delta_M + 0.3631\delta_M^2 - 0.163\delta_h^3 + 0.4586\delta_h^2\delta_M - 0.231\delta_h\delta_M^2 + 2.05 \times 10^{-15}\delta_M^3.$$

Bilaternate Product

Let A and B be $n \times n$ matrices. Let V^n be the $\frac{1}{2}n\,(n-1)$-tuple consisting of pairs of integers (p, q), $p = 2, 3 \ldots n$, $q = 1, \ldots, p-1$, listed lexicographically. That is, $V^n = [(2,1)\,,(3,1)\,,(3,2)\,,(4,1)\,,(4,2)\,,(4,3)\,,\ldots(n,n-1)]$.

Denote by V_i^n the ith entry of V^n. Denote

$$f\left((p,q)\,;(r,s)\right) = \frac{1}{2}\left(\det\begin{bmatrix} a_{pr} & a_{ps} \\ b_{qr} & b_{qs} \end{bmatrix} + \det\begin{bmatrix} b_{pr} & b_{ps} \\ a_{qr} & a_{qs} \end{bmatrix}\right),$$

where the dependence of f on A and B is kept implicit for simplicity. The bialternate product of A and B, denoted by $A \otimes B$, is a $\frac{1}{2}n\,(n-1)$-dimensional square matrix, for which the ijth entry is given by $(A \otimes B)_{ij} = f\left(V_i^n, V_j^n\right)$.

https://doi.org/10.1017/aer.2025.19 Published online by Cambridge University Press

Table A1. *Controller parameters and stabilisation intervals for Mach number changes*

i	j	$[k_p, k_d]$	(δ_M^-, δ_M^+)	$(\underline{\delta}_h, \bar{\delta}_h)$
1	1	[150, 22.5]	(−**1.489**, 0.022)	(−**1.1524**, −0.9215)
	2	[132.92, 21.24]	(−0.494, 0.441)	
	3	[119.58, 22.31]	(0.002, 0.585)	
	4	[115.53, 20.01]	(0.575, 0.723)	
	5	[100.79, 18.83]	(0.585, 0.889)	
	6	[92.79, 17.02]	(0.697, 0.942)	
	7	[88.47, 16.97]	(0.846, **1.148**)	
2	1	[145.00, 22.00]	(−**1.23**, 0.09)	(−1.0307, −0.7992)
	2	[126.86, 21.00]	(−0.42, 0.59)	
	3	[122.27, 21.94]	(0.58, 0.74)	
	4	[100.66, 20.95]	(0.59, 0.89)	
	5	[93.90, 20.35]	(0.67, 0.95)	
	6	[88.88, 19.68]	(0.85, 0.97)	
	7	[86.52, 18.70]	(0.91, 0.98)	
	8	[85.18, 19.70]	(0.94, 0.98)	
	9	[87.04, 17.14]	(0.85, **1.16**)	
3	1	[140.00, 22.50]	(−**1.32**, 0.17)	(−0.814, −0.5143)
	2	[129.86, 21.56]	(−0.73, 0.59)	
	3	[129.37, 20.39]	(0.58, 0.75)	
	4	[129.97, 19.60]	(0.57, 0.82)	
	5	[131.01, 18.15]	(0.66, 0.85)	
	6	[131.80, 19.17]	(0.76, 0.87)	
	7	[132.32, 18.82]	(0.81, 0.88)	
	8	[132.96, 18.64]	(0.88, 0.90)	
	9	[133.08, 17.80]	(0.89, **1.26**)	
4	1	[130.00, 22.50]	(−**1.08**, 0.30)	(−0.5617, −0.1206)
	2	[126.18, 21.94]	(−1.10, 0.60)	
	3	[103.04, 18.03]	(−0.81, 0.61)	
	4	[103.86, 16.92]	(−0.05, 0.62)	
	5	[100.33, 15.69]	(0.53, 0.63)	
	6	[99.74, 15.56]	(0.57, 0.74)	
	7	[97.22, 15.28]	(0.73, **1.37**)	
5	1	[130.00, 22.50]	(−**1.75**, 0.40)	(−0.1405, 0.4374)
	2	[123.83, 22.50]	(−1.78, 0.59)	
	3	[102.36, 18.02]	(−1.80, 0.62)	
	4	[80.31, 15.09]	(−1.79, 0.64)	
	5	[71.17, 13.73]	(−0.12, 0.65)	
	6	[68.15, 13.30]	(0.02, 0.65)	
	7	[67.18, 13.16]	(0.05, 0.66)	
	8	[66.88, 13.12]	(0.05, 0.66)	
	9	[66.32, 13.07]	(0.66, **1.29**)	

https://doi.org/10.1017/aer.2025.19 Published online by Cambridge University Press

Table A1. *(Continued)*

i	j	$[k_p, k_d]$	(δ_M^-, δ_M^+)	$(\underline{\delta}_h, \bar{\delta}_h)$
6	1	[100.00, 21.00]	(−**1.31**, 0.55)	(0.3688, 0.7620)
	2	[102.57, 18.32]	(−1.34, 0.60)	
	3	[110.73, 17.56]	(−1.36, 0.63)	
	4	[88.90, 15.77]	(−1.35, 0.63)	
	5	[64.71, 13.17]	(0.54, 0.66)	
	6	[56.70, 13.34]	(0.64, **1.17**)	
7	1	[90.00, 19.00]	(−**1.05**, 0.51)	(0.7542, **1.1132**)
	2	[84.12, 16.66]	(−1.09, 0.57)	
	3	[74.00, 14.05]	(0.42, 0.64)	
	4	[73.71, 14.87]	(0.61, **1.40**)	

Cite this article: Zhang T.Y., Sun M.W., Chen Z.Q. and Wang Y.S. (2025). Adaptive gain-scheduling control for hypersonic flight vehicles across wide envelopes based on Guardian map. *The Aeronautical Journal*, **129**, 2055–2081. https://doi.org/10.1017/aer.2025.19

https://doi.org/10.1017/aer.2025.19 Published online by Cambridge University Press